The air bubble entrapped under a drop impacting on a solid surface

By S. T. THORODDSEN[1], T. G. ETOH[2], K. TAKEHARA[2],
N. OOTSUKA[2] AND Y. HATSUKI[2]

[1]Mechanical Engineering, National University of Singapore, 9 Engineering Drive 1, Singapore 117576
[2]Civil and Environmental Engineering, Kinki University, Higashi-Osaka 577-8502, Japan

We present experimental observations of the disk of air caught under a drop impacting onto a solid surface. By imaging the impact through an acrylic plate with an ultra-high-speed video camera, we can follow the evolution of the air disk as it contracts into a bubble under the centre of the drop. The initial size and contraction speed of the disk were measured for a range of impact Weber and Reynolds numbers. The size of the initial disk is related to the bottom curvature of the drop at the initial contact, as measured in free-fall. The initial contact often leaves behind a ring of micro-bubbles, marking its location. The air disk contracts at a speed comparable to the corresponding air disks caught under a drop impacting onto a liquid surface. This speed also seems independent of the wettability of the liquid, which only affects the azimuthal shape of the contact line. For some impact conditions, the dynamics of the contraction leaves a small droplet at the centre of the bubble. This arises from a capillary wave propagating from the edges of the contracting disk towards the centre. As the wave converges its amplitude grows until it touches the solid substrate, thereby pinching off the micro-droplet at the plate, in the centre of the bubble. The effect of increasing liquid viscosity is to slow down the contraction speed and to produce a more irregular contact line leaving more micro-bubbles along the initial ring.

1. Introduction

The impact of drops onto a solid substrate is of practical importance in coating, cleaning and cooling of surfaces. Molten drops of metal are used in soldering, and inkjet printing is finding new applications. Recent advances include the printing of polymeric circuits and large displays, Sirringhaus *et al.* (2000), which may cut production costs drastically, making this a current area of active research. The entrapment of a small bubble under the centre of an impacting drop is unavoidable and often undesirable in the above applications. Many previous studies have shown these entrapped bubbles, e.g. Chandra & Avedisian (1991) and Thoroddsen & Sakakibara (1998), but have lacked the temporal resolution to observe their formation. Most recently these bubbles have been observed by Van Dam & Le Clerc (2004) under very small droplets, only 60 µm in diameter.

Numerical methods face a number of challenges in simulating this entrapment. Recent work by Mehdi-Nejad, Mostaghimi & Chandra (2003) illustrates some of the difficulties. The range of scales between the drop size and the thickness of the very thin air sheet is ~ 1000, and the boundary conditions at the contact line also have to be modelled, see Bussmann, Chandra & Mostaghimi (2000). Theoretical treatment
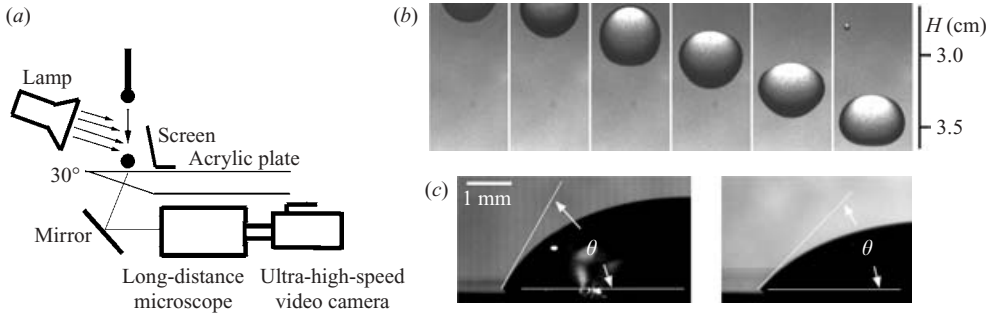
FIGURE 1. (*a*) Experimental setup, not to scale. The acrylic plate is 15 mm thick. (*b*) Drop shapes during free-fall of a water drop. (*c*) Images used to measure the static contact angle for water (left) and 80 % mass fraction of glycerin/water mixture.

has mostly focused on the deformation of the drop before contact, see Gopinath & Koch (2002).

Herein we present the first time-resolved observations of this air-entrapment process, over a wide range of impact conditions.

2. Experimental setup

2.1. *Optical setup and impact conditions*

Figure 1(*a*) shows the experimental setup. The solid substrate was in all cases a flat acrylic plate. To avoid optical distortions by the curved surface of the drop, we viewed the solid/liquid contact through the plate. Direct vertical viewing did not give sufficient contrast. To improve this we cut the plate to form a 30° wedge. We used diffuse background lighting, with a high-intensity lamp shining on a paper screen. As the light has to pass through the changing shape of the drop surface, this generates uneven background lighting. Minor adjustments of the screen and lamp were therefore required for different impact heights. We used a long-distance microscope to observe the finer details.

Experiments were conducted over a range of impact conditions. The drops were generated by a gravity-driven pinch-off from a nozzle, with the impact velocity U being varied by changing the release height H of the nozzle above the surface. Observations were performed with water, alcohol and water/glycerin mixtures. The static contact angle of water on the acrylic plate was measured as $\theta = 59°$ and that of 80 % glycerin/water mixture as $\theta = 46°$ (figure 1*c*), whereas alcohol completely wets the surface. The stainless steel needle used in most of the experiments had an inner diameter of 2.5 mm. This generated water drops of diameter $D = 4.0$ mm. For the largest Weber/Reynolds numbers (figures 2*a*, 4*a*) a larger plastic valve was used, of 5 mm OD and generated water drops of $D \simeq 5.5$ mm. This produced a total range for the Weber and Reynolds numbers, based on liquid properties, the drop diameter D and impact velocity $U = \sqrt{2g(H - D)}$, of

$$We = \frac{\rho D U^2}{\sigma} = 20\text{–}1500, \qquad Re = \frac{DU}{\nu} = 5\text{–}30000.$$

2.2. *Ultra-high-speed video camera*

The air disk contracts in a fraction of a millisecond. Detailed observations therefore required high-speed imaging, accomplished with a newly developed ultra-high-speed
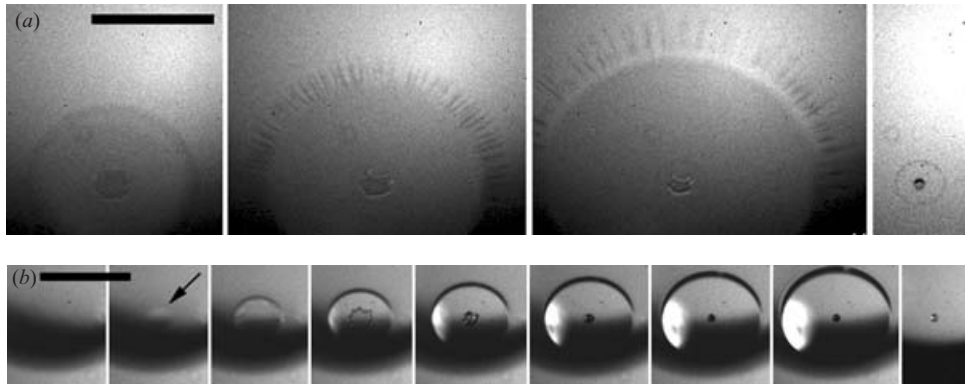
FIGURE 2. The air disks for the largest and smallest drop heights for water drops. (*a*) $H = 100$ cm and $D = 5.5$ mm, $We = 1500$, $Re = 30\,300$. The time between the first three frames $dt = 10\,\mu s$, with the last frame $600\,\mu s$ after the first. Notice the progenitors of the fingering, as discussed in Thoroddsen & Sakakibara (1998). (*b*) $H = 2.25$ cm, $D = 4.0$ mm, $We = 19$, $Re = 2920$, $dt = 20\,\mu s$, with the last frame $1120\,\mu s$ after the first. The scale bars are 1 mm long.

video camera (Etoh *et al.* 2003). Most of the results presented herein are taken at frame-rates between 20–100 kHz. The camera uses simultaneous parallel recording of all pixels, using memory within every pixel. The prototype (Shimadzu Corp.) can acquire 103 consecutive frames, with each frame having 260×312 pixel elements irrespective of the frame rate used. Thoroddsen, Etoh & Takehara (2003) have previously used this camera to study the entrapment of air bubbles under a drop impacting onto a flat liquid surface. The triggering is based on the drop cutting a laser-beam/photo-diode setup. Slight sideways motions of the drops, during free-fall, introduce as much as a 1 ms inaccuracy in this trigger timing. Numerous impacts may therefore be needed to catch the first contact.

3. Results

Figures 2 and 3 show numerous impact sequences, for different liquids and impact conditions. The contraction of the air disk can take as little as $60\,\mu s$. The outer extent of the liquid contact gives an indication how close to the initial contact the first frame has been captured. In a few of the clips, for the smallest impact heights, one can observe an initial 'shadow' which we interpret as deformation of the drop taking place before contact, e.g. shown by the arrow in panel 2 of figure 2(*b*). Only for the larger $Re \geqslant 7000$ (figure 2*a*) did we observe the characteristic fingering of the lamellar jet, as described in Thoroddsen & Sakakibara (1998). The edges of the air disks often develop azimuthal serrations during the contraction and often leave a faint ring of micro-bubbles marking the original line of contact, like in the last panel of figure 2(*a*).

3.1. *Initial diameter of the air disk*

Figure 4(*a*) shows the initial size of the air disk, caught under a water drop, vs. impact Reynolds number Re. The size of the disk shows large variation, which depends primarily on the phase of oscillation of the drop, which at the high We herein is large following the pinch-off. The largest air disks are entrapped when the bottom of the drop is flattest. Some of the bottom radii of curvature R_{bc} were measured in a separate experiment, using images like those in figure 1(*b*). Figure 4(*b*) shows the R_{bc} around the large spike in figure 4(*a*). The aim here is not to track the effects of every
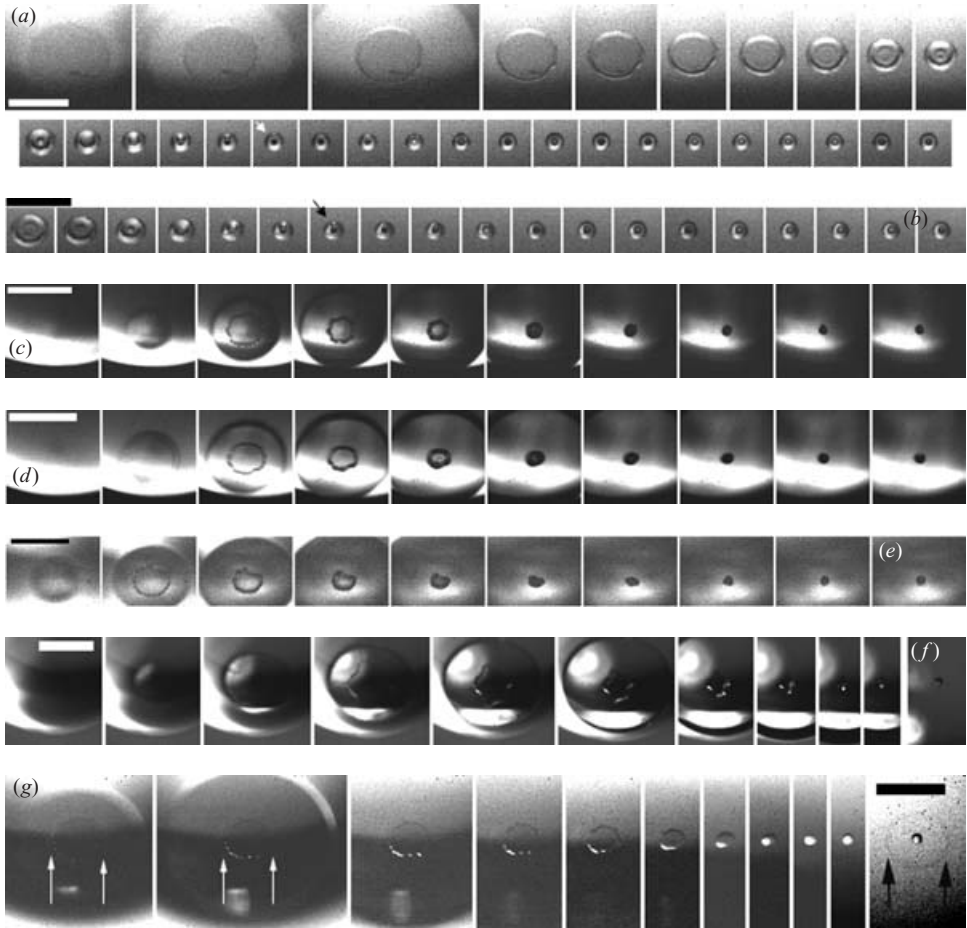
FIGURE 3. Contraction of the air disk, for various impact conditions. (*a–e*) Water drops $D = 4.0$ mm. (*a*) $H = 9.7$ cm, $We = 102$, $Re = 6740$, d$t = 10$ μs. (*b*) Images from another clip under the same conditions. The arrows point to a trumpet-shaped neck which subsequently pinches off to form a microdrop at the centre, as sketched in figure 8. (*c, d*) Two realizations for $H = 4.4$ cm, $We = 44$, $Re = 4420$, d$t = 10$ μs. (*e*) $H = 8.2$ cm, $We = 86$, $Re = 6170$, d$t = 10$ μs. (*f*) Drop of alcohol, $H = 2.5$ cm, $D = 3.1$ mm, $We = 50$, $Re = 1325$, with d$t = 20$ μs. (*g*) More viscous drop, 80% glycerin/water mixture, $H = 11.2$ cm. $We \simeq 160$, $Re \simeq 100$. Times shown are 0, 20, 40, 60, 80, 120, 160, 220, 320, 720, 2000 μs. The white arrows point out the location of the edge and the dark arrows point at a faint outer ring of micro-bubbles left behind. The scale bars are 500 μm long.

minute change in the bottom curvature of the falling drop, but to verify the proposed dependence, for the extreme case. For the data in figure 4(*b*) ($Re \sim 4000$, $We \sim 30$) we find the initial radius of the air disk, $R_i = (0.16 \pm 0.04) R_{bc}$. The largest air disks have an initial diameter of 1.8 mm and are observed for $H = 3.55$ cm. Figure 1(*b*) shows that the bottom of the drop in this case is close to being flat.

3.2. *Speed of contraction of the air disk*

Following the ideas in Thoroddsen *et al.* (2003, 2005), see also Oguz & Prosperetti (1989) and Eggers, Lister & Stone (1999), we construct a model of the contraction speed, where the radial velocity of the edge represents a balance between surface
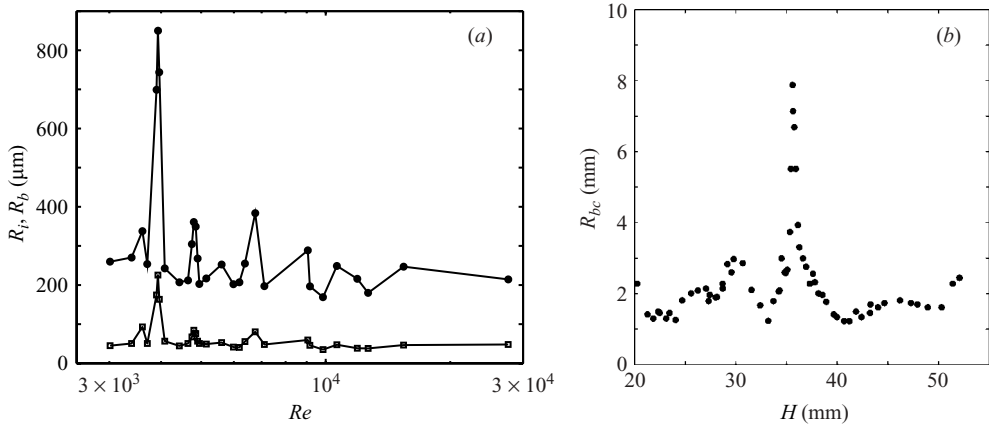
FIGURE 4. (*a*) The initial radius R_i of the air disk (●) and the radius of the bubble R_b after it contracts (□) vs. *Re*, for water drops of $D = 4.0$ mm and *H* from 2.25 to 100 cm. The corresponding *We*, range from 19 to 1500. (*b*) The bottom radius of curvature of the drop R_{bc} in free-fall (figure 1*b*), vs. the release height from the nozzle *H*. The peak coincides (± 0.5 mm) with the largest disks in (*a*).
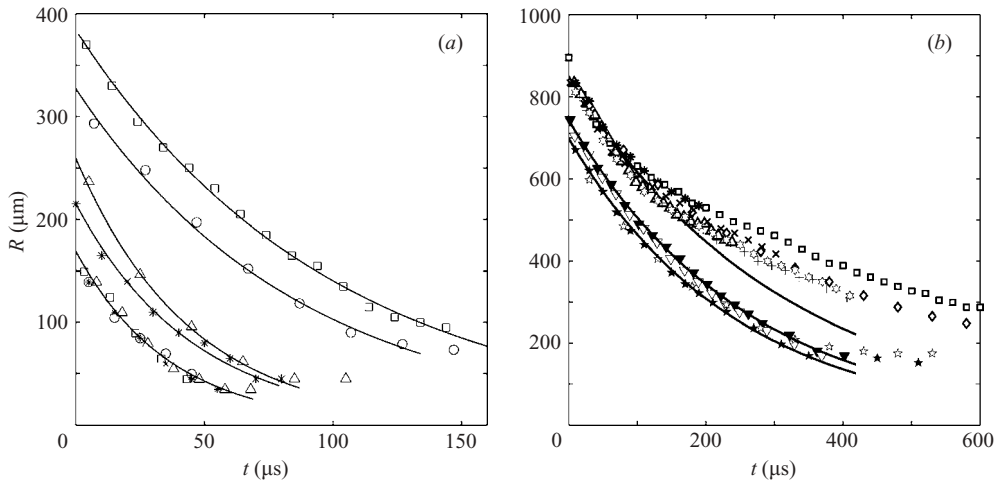

FIGURE 5. The contraction of typical air-disks vs. time, for water drops $D = 4.0$ mm. (*a*) From bottom to top the curves are for $H = 20.2$, 100, 2.25, 5.0 and 9.7 cm. (*b*) Contraction of the largest air disks, for the three largest R_i in figure 4(*a*), which occur for slightly different release heights of $H = 3.5$ (★, $C = 1.18$), 3.55 (other symbols, $C = 1.35$) and 3.6 cm ($\triangledown$, ▼, $C = 1.02$).

tension σ and inertia, i.e. $u = \mathrm{d}R/\mathrm{d}t \sim -\sqrt{\sigma/(\rho\delta)}$, where δ is the instantaneous average thickness of the air sheet and ρ is the liquid density. This gives the time-evolution of the disk radius

$$R(t) = R_i \exp(-C\sqrt{\pi\sigma/(\rho V)}\,t) \tag{3.1}$$

where $\delta = V/(\pi R^2)$ has been deduced from the total volume of air in the bubble V and C is a proportionality constant. In Thoroddsen *et al.* (2003) for an air disk caught under a drop impacting onto a liquid surface, $C = 0.94 \pm 0.13$.

Figure 5 shows that the contraction along a solid surface also follows an exponential curve. Figure 6(*a*) shows the corresponding values of C. However, in finding the value
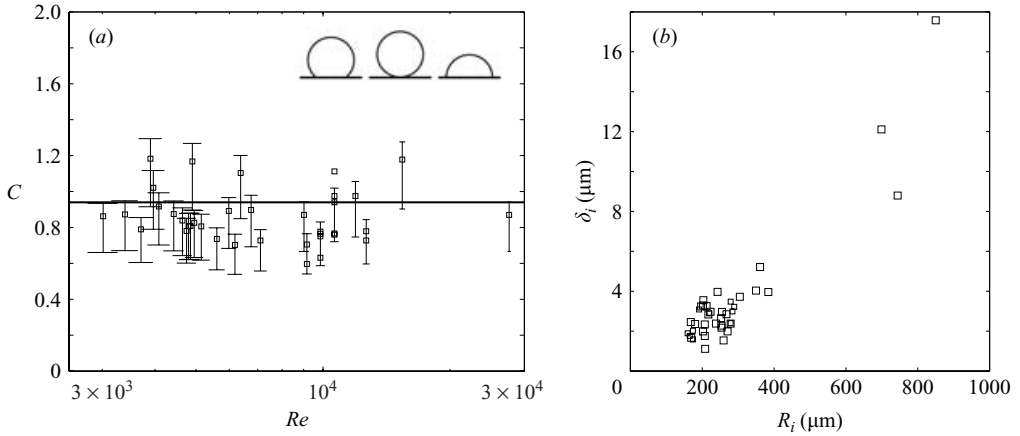
FIGURE 6. (a) The best-fit values of C in (3.1) for water drops $D = 4.0$ mm. The horizontal line shows the average value of $C = 0.94$, obtained by Thoroddsen *et al.* (2003) for drop–liquid impacts. Top right: bubble shapes after contraction of the air sheet, used to calculate error bars, through the entrapped air volume. (b) δ_i vs. R_i for the same data.

of C we face the difficulty that the total amount of air is not easily measured, due to the unknown contact angle. We can assume the contact line has reached the static contact angle, but this may not occur during the first millisecond after contact, even though the fast motions have subsided. We therefore include a range of C around this value, accounting for the air volume, from a maximum of a sphere to the minimum of a hemisphere.

The data show considerable scatter, with no clear trend in this range of Re. The average value of $C = 0.88$, with an r.m.s. variation of 0.14, is quite close to the average for drop–liquid impacts, shown by the horizontal line.

The largest disks, for $H = 3.55$ cm in figure 5(b), contract more slowly than predicted by (3.1), with the largest of the disks contracting the slowest. We believe this is caused by excess air caught in a dimple at the centre. In comparison, the slightly smaller entrapped disks, for $H = 3.5$ and 3.6 cm, follow closely exponential curves.

Figure 6(b) shows a clear correlation between the average initial thickness of the air sheet δ_i and the initial size of the disk R_i. Figure 4 showed that R_i is related to the bottom radius of curvature R_{bc}, but our limited data for R_{bc} cannot decouple the effects of We and R_{bc} over the full range of H.

Figure 3(f) shows the contraction for an alcohol drop. Here the contact line appears more unstable, forming larger serrations at the edge. For alcohol, we can get an accurate estimate of the air volume, as it fully wets the acrylic substrate and the bubble separates from the surface. This was verified in an anomolous clip, where the impact was asymmetric and the bubble drifted with the average flow. For the parameter range studied for alcohol drops ($We \sim 70$–900, $Re \sim 1600$–5800), we find from a handful of realizations that $C = 0.79 \pm 0.14$. For these conditions the average initial thickness of the air disk δ_i becomes $(4/3)(R_b^3/R_i^2) = 1.9$ μm.

3.3. Capillary waves and centre contact

Figure 7(a) shows that the capillary waves propagate from the edges of the contracting sheet towards the centre. Figure 8 shows the proposed evolution, as the waves converge and their amplitude grows until the crest touches the substrate, pinching off a small
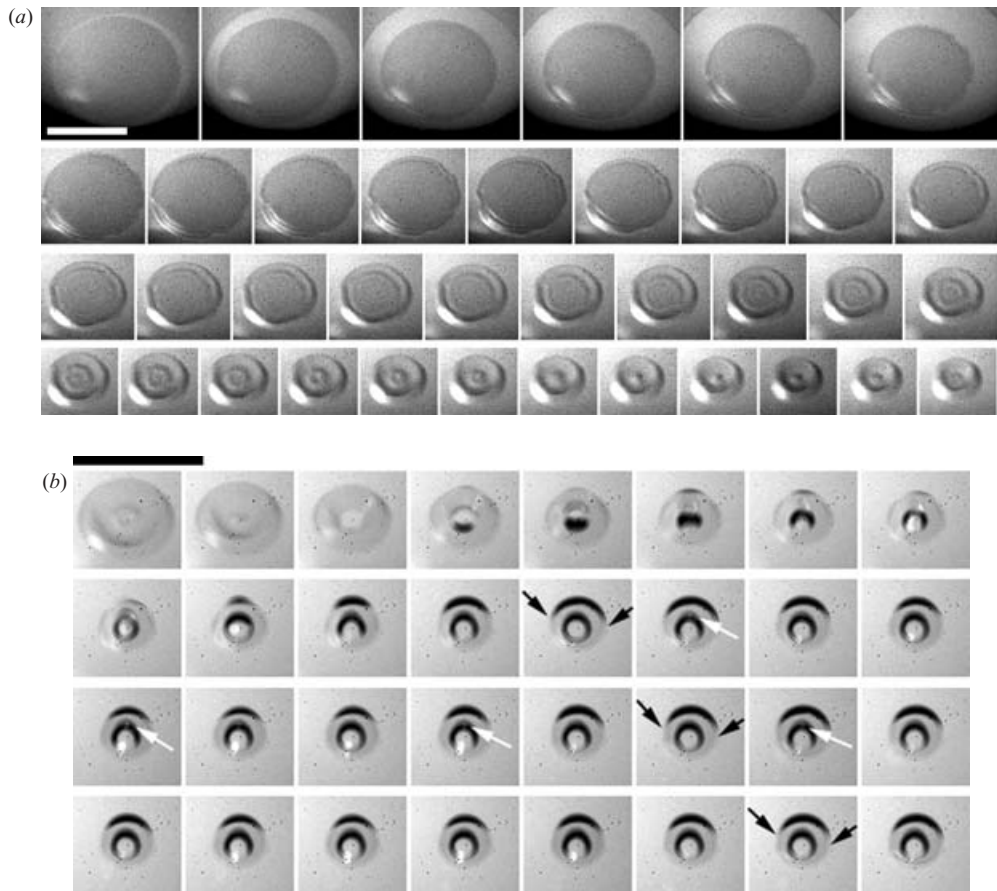
FIGURE 7. (*a*) Capillary waves on the surface of the contracting layer of air, for $H = 3.55$ cm, $We = 34$ and $Re = 4200$. This clip ends just before the wave makes contact with the substrate, $dt = 10\,\mu$s. (*b*) The pinch-off and the subsequent oscillations of the microdrop and the bubble, $dt = 50\,\mu$s. Both scale bars are 1 mm.
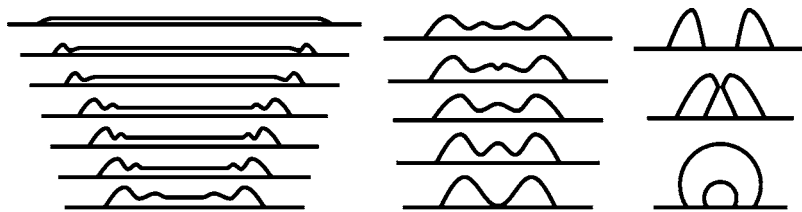

FIGURE 8. Sketch (based on figure 7) of the proposed pinch-off of a droplet inside the bubble, with arbitrary, but greatly exaggerated, vertical scale.

droplet at the centre of the bubble. With the pinned contact lines, it is not obvious that minimization of the surface energy would promote this pinch-off over a toroidal surface, but the pinch-off is clearly supported by the oscillations observed in the clips. This is shown in figure 7(*b*). The centre contact of the capillary wave with the solid surface occurs in the third frame and the pinch-off takes place in the eighth frame. Following this pinch-off the two surfaces oscillate with different frequencies. This is
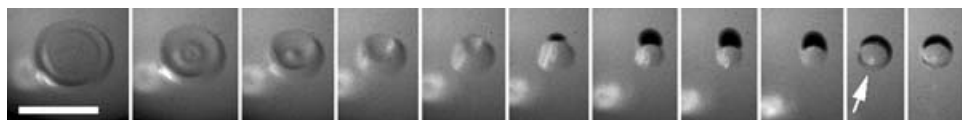
FIGURE 9. Realization where the centre does not touch the plate, for the same impact conditions as in figure 7. The first nine panels are $100\,\mu s$ apart with the last two at 1080 and $2020\,\mu s$ after the first panel. Scale bar is 1 mm.

more easily observed in the moving images than from the sequence of still frames. We therefore point out repeated patterns associated with the oscillations. The extent of the top arch changes during the oscillation of the bubble surface. This arch reaches maximum length every ninth frame, as marked by the dark arrows. This corresponds to a frequency of 2200 Hz. The oscillations of the micro-drop are much faster, as revealed by a bright spot at its top, marked by the white arrows. This spot appears at intervals of $150\,\mu s$, giving a frequency of 6700 Hz. A video clip taken under the same impact conditions is available as a supplement to the online version of this paper.

These values can be compared to the oscillation frequencies of an inviscid drop, Lamb (1932, §275), where $\omega_n^2 = n(n-1)(n+2)\,\sigma/(\rho\,R^3)$, which for a water drop of the measured radius, $R = 110\,\mu m$, gives a frequency of $\omega_3/2\pi = 6450$ Hz for mode 3, which we have selected due to the pinned equator. Similarily, for a bubble of $R = 220\,\mu m$, $\omega_n^2 = (n+1)(n-1)(n+2)\,\sigma/(\rho\,R^3)$, which gives $\omega_3/2\pi = 2600$ Hz. Both of these values are reasonably close to the observations and support our conclusion that the micro-drop is indeed pinched off inside the bubble. Figure 3(a, b) shows a similar pinch-off for smaller air-disks. Here the micro-droplets have radii of only $35\,\mu m$.

Figure 8 sketches the proposed pinch-off evolution. The neck above the micro-droplet is visible in the arrowed frames in figure 3(a, b). Due to the complicated optical paths and curved liquid surfaces, it is sometimes not obvious which features produce the intensity pattern in the images. To further demonstrate that the centre-drop in figures 3(a, b) and 7 is not an optical illusion, we include in figure 9 the one realization where the capillary wave did not touch the plate at the centre of the bubble, therefore producing no micro-drop at its centre. Notice also the large light spot/ring to the lower left, which is light focused by passing through the top of the drop. The arrow points to a much smaller light ring formed by the light passing through the top of the entrapped bubble.

Once the speed of contraction has slowed down, the capillary waves overtake the edge and propagate towards the centre. The speed of propagation can be roughly estimated, as $u = 3\,m\,s^{-1}$ (from the fifth to last frames in the third row of figure 7a). This is close to the group velocity for the measured wavelength, $\lambda = 140\,\mu m$, i.e. $c_g = 1.5\,\sqrt{2\pi\,\sigma/(\rho\lambda)} = 2.7\,m\,s^{-1}$, keeping in mind that the estimate of λ is quite inaccurate. This supports the capillary nature of these waves.

3.4. *The effect of changing liquid viscosity*

The effect of viscosity was investigated using glycerin/water mixtures. Figure 10(a) shows how increased viscosity slows down the contraction speed of the air-disk. For the smallest Reynolds number, based on the viscous time scale (Eggers *et al.* 1999), i.e. $Re_\mu = \rho R_{drop}\sigma/\mu^2 \simeq 1$, the motion proceeds at a constant velocity $u = 0.28\,m\,s^{-1} \simeq 2.6\sigma/\mu$.

Figure 10(b) shows the reduction in C with increasing liquid viscosity, determined from best-fit exponential curves to data similar to those shown in figure 10(a). These changes are shown in terms of the Ohnesorge number $Oh = \mu/\sqrt{D\sigma\rho}$. The reduction
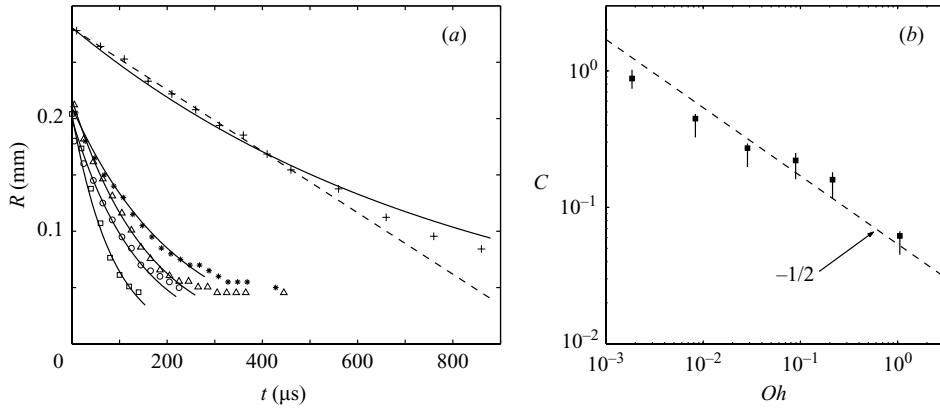
FIGURE 10. The effect of viscosity on the contraction speed. (*a*) Best-fit exponential curves for 50 % to 99 % glycerin/water mixtures. The corresponding dynamic viscosities are $\mu = [4.5$ ($\square$), 16 ($\bigcirc$), 50 ($\triangle$), 121 ($\ast$) and 602 ($+$)] $\times 10^{-3}$ Ns m^{-2}. (*b*) The best-fit C-values vs. Oh.
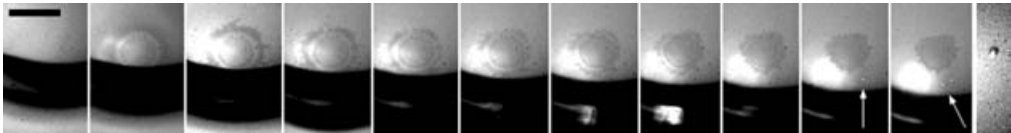

FIGURE 11. Impact of a 99 % glycerin drop, with $We = 136$ and $Re = 8$. Frames are spaced by d$t = 50$ μs, with last frame 2100 μs after the first. Scale bar is 500 μm. The contrast is particularly faint, as the refractive index of the glycerin is close to that of the plate.

in speed can roughly be approximated as $C \propto 1/\sqrt{Oh}$. The average thickness of the air disk for the more viscous liquids is around 2 μm.

For the largest viscosity the air disk resembles a fried egg, figure 11, with a prominent brighter ring around the centre region, and an irregular region of air at the periphery. The whole region appears to be connected, without touching the surface, as it all contracts into a central bubble. From watching the contraction, it appears that the lighter ring represents a thinner layer of air, but more detailed study is required to explain its formation. The outer irregular region leaves myriad micro-bubbles behind, some of which are visible by their bright reflections marked by arrows in the later frames.

4. Discussion and conclusions

These measurements show that the contraction velocity is very similar to the corresponding case of an air disk caught when a water drop impacts onto a liquid surface. This suggests that the dynamics are governed by the contraction of the air-disk to minimize surface energy, rather than wetting of the liquid along the surface, which would be a much slower process. The initial ring of micro-bubbles is also consistent with this view. The no-slip condition at the wall should increase viscous shear forces, but for water this does not appear to be dominant.

The air disks are significantly thicker herein, $\delta_i \sim 2$–5 μm, than in the drop–liquid case, Thoroddsen *et al.* (2003), where $\delta_i \sim 1$–2.5 μm. We can speculate that the compliance of the liquid surface allows more time for air drainage from the sheet before contact. The no-slip boundary condition at the air–solid interface may also play a role.

The fact that the normalized contraction speeds, i.e. C-values in the model, are similar for the water ($\theta = 59°$) and alcohol, which wets the acrylic plate, suggests that the wettability of the liquid does not affect the contraction of the air disk, as it occurs much faster than typical wetting, de Gennes (1985). Experiments by Biance, Clanet & Quéré (2004) show the same to be true for the initial capillary–inertial regime of wetting for a drop touching a glass plate, where they find the speed to be the same whether the plate is dry or wet. They propose that a microscopic precursor film makes the dynamics independent of the spreading parameter. Our model of the contraction speed does not include the dynamic contact angle at the plate and is based on the average thickness of the air sheet, whereas a thicker edge can be seen to develop. However, here this edge has negligible inertia, in contrast with the rupture waves described by Taylor (1959) and Rozhkov, Prunet-Foch & Vignes-Adler (2002).

The ring of micro-bubbles left at the initial contact radius (figure 2a) might therefore occur before this precursor film has been established. However, the largest radial velocity occurs at the onset of the contraction $u \simeq C\sqrt{\sigma/(\rho\delta_i)} \simeq 5\,\mathrm{m\,s}^{-1}$, which for water gives a capillary number $Ca = \mu U/\sigma \simeq 0.07$, far below the critical Ca for dynamic wetting, Jacqmin (2002). This suggests that the initial contact might be irregular in the azimuthal direction, thereby entrapping the initial ring of micro-bubbles.

Serrations appear on the contact line, with their number decreasing during the contraction, for example going from about 20 to 10 in 10 µs, see figure 3(c), frames 3 to 4. This is reminiscent of the results in Thoroddsen et al. (2003) for capillary instability at the thicker edge, but the dynamics must be different here owing to the presence of the contact line. Even faster imaging and larger magnifications are needed to observe the details of the evolution of the edge and the effects on it of wettability and surface roughness.

In conclusion, we have presented the first time-resolved imaging of the entrapment of an air-disk caught under a drop impacting onto a solid surface, measuring its contraction speed and discovering an intriguing capillary phenomenon, where a micro-droplet is pinched off inside the entrapped bubble.

REFERENCES

BIANCE, A.-L., CLANET, C. & QUÉRÉ, D. 2004 *Phys. Rev. E* **69**, paper 016301, 1–4.
BUSSMANN, M., CHANDRA, S. & MOSTAGHIMI, J. 2000 *Phys. Fluids* **12**, 3121–3132.
CHANDRA, S. & AVEDISIAN, C. T. 1991 *Proc. R. Soc. Lond.* A **432**, 13–41.
EGGERS, J., LISTER, J. R. & STONE, H. A. 1999 *J. Fluid Mech.* **401**, 293–310.
ETOH, T. G., POGGEMANN, D., KREIDER, G. *et al.* 2003 *IEEE Trans. Electron Devices* **50**, 144–151.
DE GENNES P. G. 1985 *Rev. Mod. Phys.* **57**, 827–863.
GOPINATH, A. & KOCH D. L. 2002 *J. Fluid Mech.* **454**, 145–201.
JACQMIN, D. 2002 *J. Fluid Mech.* **455**, 347–358.
LAMB, H. 1932 Hydrodynamics. *Cambridge University Press.*
MEHDI-NEJAD, V., MOSTAGHIMI, J. & CHANDRA, S. 2003 *Phys. Fluids* **15**, 173–183.
OGUZ, H. N. & PROSPERETTI, A. 1989 *J. Fluid Mech.* **203**, 149–171.
ROZHKOV, A. PRUNET-FOCH, B. & VIGNES-ADLER, M. 2002 *Phys. Fluids* **14**, 3485–3501.
SIRRINGHAUS, H., KAWASE, T., FRIEND, R. H. *et al.* 2000 *Science*, **290**, 2123–2126.
TAYLOR, G. I. 1959 *Proc. R. Soc. Lond.* A **253**, 313–321.
THORODDSEN, S. T., ETOH, T. G. & TAKEHARA, K. 2003 *J. Fluid Mech.* **478**, 125–134.
THORODDSEN, S. T. & SAKAKIBARA, J. 1998 *Phys. Fluids* **10**, 1359–1374.
THORODDSEN, S. T., TAKEHARA, K. & ETOH, T. G. 2005 *J Fluid Mech.* **527**, 85–114.
VAN DAM, D. B. & LE CLERC, C. 2004 *Phys. Fluids* **16**, 3403–3414.